Tracking Structural Phase Transitions in Lead-Halide Perovskites by Means of Thermal Expansion

Masoumeh Keshavarz,* Martin Ottesen, Steffen Wiedmann, Michael Wharmby, Robert Küchler, Haifeng Yuan, Elke Debroye, Julian A. Steele, Johan Martens, Nigel E. Hussey, Martin Bremholm, Maarten B. J. Roeffaers, and Johan Hofkens*

The extraordinary properties of lead-halide perovskite materials have spurred intense research, as they have a realistic perspective to play an important role in future photovoltaic devices. It is known that these materials undergo a number of structural phase transitions as a function of temperature that markedly alter their optical and electronic properties. The precise phase transition temperature and exact crystal structure in each phase, however, are controversially discussed in the literature. The linear thermal expansion of single crystals of $APbX_3$ (A = methylammonium (MA), formamidinium (FA); X = I, Br) below room temperature is measured using a high-resolution capacitive dilatometer to determine the phase transition temperatures. For δ-$FAPbI_3$, two wide regions of negative thermal expansion below 173 and 54 K, and a cascade of sharp transitions for $FAPbBr_3$ that have not previously been reported are uncovered. Their respective crystal phases are identified via powder X-ray diffraction. Moreover, it is demonstrated that transport under steady-state illumination is considerably altered at the structural phase transition in the MA compounds. The results provide advanced insights into the evolution of the crystal structure with decreasing temperature that are essential to interpret the growing interest in investigating the electronic, optical, and photonic properties of lead-halide perovskite materials.

The success of hybrid organic–inorganic perovskites (HOIP) in photovoltaic applications is based on their high power conversion efficiencies, up to 23.3%, in combination with seemingly low production costs.[1–4] Owing to their remarkable photo-physical properties such as low exciton binding energies,[5,6] high absorption coefficients,[7] extended carrier lifetimes, and diffusion lengths,[8,9] HOIPs are considered as viable candidate materials for the next generation of photovoltaic devices.

The basic formula unit of the HOIPs is ABX_3, where A is the organic ammonium cation (methylammonium (MA): $CH_3NH_3^+$ or formamidinium (FA): $NH_2CH = NH_2^+$), B is the inorganic cation (here Pb), and X is the halide (here Br or I). In view of the intense ongoing investigation of the electronic and optical properties, their temperature-dependent charge carrier dynamics and intrinsic scattering processes, it is of fundamental interest to precisely explore the evolution of the perovskite crystal structure with temperature. In order to elucidate the miscellany of the so far reported crystal phases and transition temperatures, in particular in the FA-based HOIPs, we use thermal expansion to accurately determine the temperature evolution of the crystal structure. A change in the crystal structure has severe consequences for the electronic properties of each material including changes in the band structure and thus in the band

Dr. M. Keshavarz, Dr. H. Yuan, Dr. E. Debroye, Prof. J. Hofkens
Molecular Imaging and Photonics
Department of Chemistry
Katholieke Universiteit Leuven
Celestijnenlaan 200F, 3001 Leuven, Belgium
E-mail: masoumeh.keshavarz@kuleuven.be;
johan.hofkens@kuleuven.be
M. Ottesen, Dr. M. Bremholm
Department of Chemistry and iNANO
Aarhus University
Langelandsgade 140, 8000 Aarhus C, Denmark
Dr. S. Wiedmann, Prof. N. E. Hussey
High Field Magnet Laboratory and Institute for Molecules and Materials
Radboud University
Toernooiveld 7, 6525 ED Nijmegen, Netherlands

The ORCID identification number(s) for the author(s) of this article can be found under https://doi.org/10.1002/adma.201900521.

Dr. M. Wharmby
Deutsches Elektronen-Synchrotron (DESY)
Notkestr. 85, 22607 Hamburg, Germany
Dr. R. Küchler
Max Planck Institute for Chemical Physics of Solids
Nöthnitzer Str. 40, 01187 Dresden, Germany
Dr. J. A. Steele, Prof. M. B. J. Roeffaers
cMACS
Department of Microbial and Molecular Systems
KU Leuven
Celestijnenlaan 200F, 3001 Leuven, Belgium
Prof. J. Martens
Department of Microbial and Molecular Systems
Centre for Surface Chemistry and Catalysis (COK-KAT)
KU Leuven
Celestijnenlaan 200F, 3001 Leuven, Belgium

**ADVANCED
SCIENCE NEWS**

www.advancedsciencenews.com

**ADVANCED
MATERIALS**

www.advmat.de

gap, which consequently alters their optical properties.[10,11] Furthermore, a structural phase transition may also lead to changes in the phonon structure that in turn influences the exciton binding energy due to a change in the dielectric constant.[12–14] Another important question that arises is whether and how the charge transport properties under steady-state illumination are altered, and whether the temperature-dependent charge carrier mobility is still a good means of identifying the underlying scattering mechanisms of the charge carriers by phonons.[15,16]

Long before lead-halide perovskites were identified as candidate materials for photovoltaic applications, their structural phase transitions and corresponding entropies were investigated using temperature-dependent X-ray diffraction (XRD),[17] measurements of the temperature-dependent complex permittivity[17] as well as calorimetric and spectroscopic studies,[18] with a focus on the dynamic disorder of the methylammonium group within the high-temperature phase(s). The structural phase transitions found in refs. [17,18] in MAPbI$_3$ and MAPbBr$_3$ are summarized in Table S1 in the Supporting Information.

In this work, we measure the linear thermal expansion $\Delta L/L$ of the tri-halide perovskites MAPbI$_3$, δ-FAPbI$_3$, MAPbBr$_3$, and FAPbBr$_3$ using capacitive dilatometry between 4.2 and 280 K. In MAPbI$_3$ and MAPbBr$_3$, we determine all phase transition temperatures until we reach the orthorhombic phase at low temperatures. The linear thermal expansion in δ-FAPbI$_3$ and FAPbBr$_3$ is found to be extremely complex compared to their MA counterparts. FAPbBr$_3$ exhibits several sharp transitions between 120 and 160 K while δ-FAPbI$_3$ is distinct and shows negative linear thermal expansion across temperature intervals below 173 and 54 K. Single-crystal and powder XRD (SCXRD and PXRD) were used to follow the evolution of the lattice parameters. SCXRD verified both the overall trend and the large thermal expansion observed in both compounds. Via PXRD, we determined the change of the crystal phase in δ-FAPbI$_3$ at 173 K from the space group $P6_3/mmc$ to $P6_3/m$. For FAPbBr$_3$, a decrease in symmetry was observed in both PXRD and SCXRD upon cooling from 300 to 100 K. Two phase transitions were detected for FAPbBr$_3$ at 250 and 165 K from cubic to tetragonal and from tetragonal to orthorhombic, respectively. Structural phase transitions in general affect not only the optical and photonic response[10–14] but also the charge transport properties under steady-state illumination as we demonstrate in subsequent transport measurements on MAPbI$_3$ and MAPbBr$_3$.

The volume thermal expansion coefficient $\beta = -1/V(\partial S/\partial T)_P$, where S denotes the entropy at constant pressure P, is a measure of the relative change in a sample's volume, V, and is a powerful tool to probe various kinds of phase transitions. Compared to other thermodynamic probes, such as heat capacity, thermal expansion quantifies the directional dependence of the crystal structure by measuring the linear thermal expansion $\Delta L(T)/L$ or the linear coefficient $\alpha = -1/L(dL/dT)_P$ along different crystallographic axes. For all halide perovskite materials under investigation, we have performed temperature sweeps on different bulk single crystals, determined $\Delta L(T)/L$,[19,20] and normalized it to the reference temperature, e.g., at 280 K, i.e., $\Delta L/L$ (280 K) = 0.

Let us first focus on the MA-based lead-halide perovskite materials, to date the most studied compounds in the tri-halide perovskite family. The results of the thermal expansion using capacitive dilatometry are summarized in **Figure 1**. Let us first consider MAPbI$_3$. Figure 1a shows the linear thermal expansion, $\Delta L/L$, and the linear thermal expansion coefficient, α, as a function of temperature T. $\Delta L/L$ increases monotonically in the entire temperature range but exhibits a sharp step at $T^P = 160.9$ K that we identify as the orthorhombic to tetragonal phase transition, see inset of Figure 1a.[21–23] In Figure 1b, we show the longitudinal resistance R_{xx}, measured in a Hall-bar geometry, of a MAPbI$_3$ single crystal under steady-state illumination as a function of temperature (for details see the Experimental Section). The resistance decreases by a factor of two from room temperature down to 161 K. Precisely at T^P, R_{xx} abruptly rises by one order of magnitude before decreasing again markedly with decreasing temperature in the orthorhombic regime. The sharpness of the transition observed in transport is reminiscent of the one observed in the linear thermal expansion. However, the behavior of R_{xx} with decreasing temperature deserves particular attention. First, below T^P, R_{xx} decreases gradually with temperature down to 80 K and then appears to saturate. Second, as indicated by the dashed line in Figure 1b, we find that the overall decrease of R_{xx} in temperature is metallic ($dR_{xx}/dT > 0$) down to 25 K if one neglects the feature associated with the structural phase transition. Below 25 K, R_{xx} exhibits an upturn, which is attributed to thermally activated hopping of charge carriers.[16] The transition from the tetragonal to the cubic phase occurs above 320 K,[18] a feature recently investigated by a thermomechanical analysis.[24]

We now turn to consider the experimental results obtained for MAPbBr$_3$ that are presented in Figure 1c. Compared to MAPbI$_3$, the change of the halide from I to Br has consequences on the observed structural phase transitions that, as discussed in the Supporting Information, also depend on the quality of the crystals, as exemplified by the two batches referred to here as batch A and B (the latter having the higher defect concentration, see Supporting Information). MAPbBr$_3$ is known to exhibit three structural phase transitions between 4.2 and 280 K as summarized in Table S1 in the Supporting Information and refs. [17,18]. The T-dependence of the linear thermal expansion and the thermal expansion coefficient α for batch A are illustrated in Figure 1c. $\Delta L/L$ first slowly increases up to around 147 K with increasing T. Then, $\Delta L/L$ undergoes two step-like transitions at 149.3 and 154.9 K. These steps appear as maxima in $\alpha(T)$, as shown in Figure 1d–f, and are identified as transitions from the orthorhombic (OR) to the tetragonal-II (TG (II)) phase at $T^P = 149.3$ K, and from the tetragonal-II to the tetragonal-I (TG (I)) phase at $T^P = 154.9$ K, respectively.[17,18] In the tetragonal-I phase, $\Delta L/L$ first increases monotonically before experiencing a strong pronounced increase at 235 K, which we identify as the transition from the tetragonal-I to the high-temperature cubic phase. For $T > 235$ K, $\Delta L/L$ continues to increase with increasing temperature. Samples from batch B exhibit a different behavior as highlighted in the Supporting Information (Figures S1 and S2, Supporting Information). Based on this observation, it would appear that disorder plays an important role in defining the
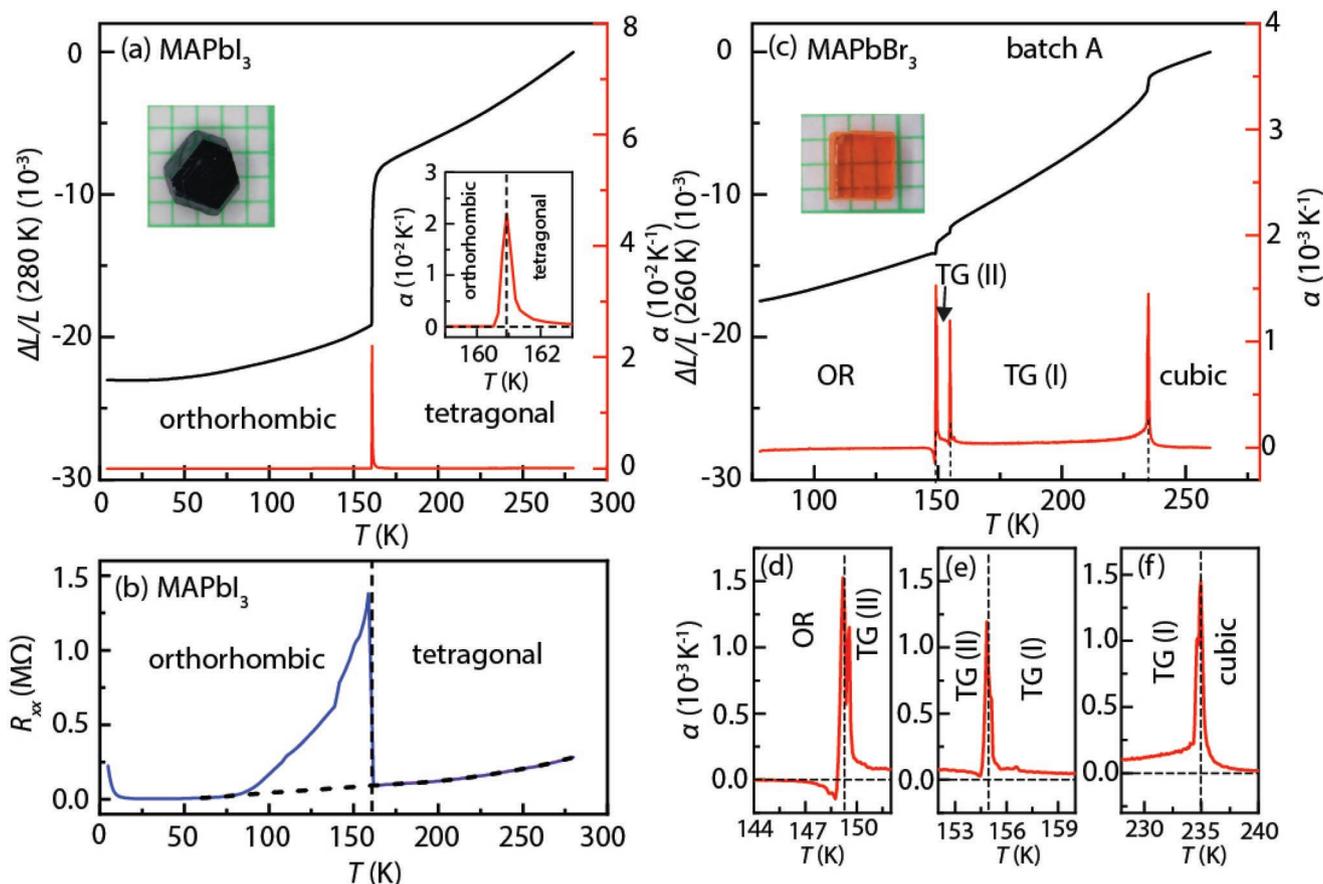
Figure 1. Observation of the structural phase transitions in MAPbI$_3$ and MAPbBr$_3$. a) $\Delta L/L$ for MAPbI$_3$ and linear thermal expansion coefficient α as a function of temperature. The phase transition from an orthorhombic to a tetragonal phase is found at 160.9 K, see inset for $\alpha(T)$. b) Longitudinal resistance R_{xx} under steady-state illumination as a function of temperature. The horizontal dashed line indicates the temperature dependence of R_{xx} in the absence of the structural phase transition. c) $\Delta L/L$ and α as a function of temperature for MAPbBr3 (batch A). d–f) Zoom of the thermal expansion coefficient α in the vicinity of the tetragonal phases, see Table S1 in the Supporting Information. OR: orthorhombic, TG (I): tetragonal-I, and TG (II): tetragonal-II.

underlying crystal structure and thereby, the electronic (see Figure S2, Supporting Information) and optical properties of MAPbBr$_3$.

Having demonstrated that linear thermal expansion is a powerful technique to probe the evolution of the crystal structure and to precisely determine phase transition temperatures, we now turn our attention to the FA-based lead-halide perovskite materials. In contrast to the MA-based HOIPs, there are only a few experimental studies that address the low-temperature structural phase transitions in FA compounds. Here, we show that the change from MA to the smaller organic ammonium cation, FA, results in profound changes in the linear thermal expansion. The results obtained for δ-FAPbI$_3$ and FAPbBr$_3$ are presented in **Figures 2** and **3** with the phase transition temperatures and phases specified in **Tables 1** and **2**, respectively. It should be noted that previous studies of the crystal structure as derived from variable temperature single crystal/powder XRD studies of FAPbBr$_3$ gave contradictory conclusions.[25,26] We first focus on δ-FAPbI$_3$ in Figure 2a. In contrast to all other materials investigated here, δ-FAPbI$_3$ does not exhibit abrupt transitions in $\Delta L(T)/L$. Instead, two regions of negative thermal expansion (NTE), highlighted by the boxes in Figure 2a, are

found that are superimposed on a positive thermal expansion background with decreasing temperature. The first region of NTE is found below $T^P = 173$ K, while the second is observed below 54.5 K, after which $\Delta L/L$ increases markedly with decreasing temperature. Both transitions are also clearly identified in $\alpha(T)$.

NTE is generally associated with materials that exhibit ferroelectric, magnetic, or charge-transfer phase transitions that cause the material to contract upon increasing temperature due to either a redistribution or an ordering of ferroelectric/-magnetic domains.[27] The first region of NTE in δ-FAPbI$_3$ is found between 173 and 150 K with a thermal expansion coefficient $\alpha \approx -1.3 \times 10^{-4}$ K^{-1}. The low-temperature NTE, on the other hand, exhibits a remarkably large value of $\alpha \approx -2.5 \times 10^{-4}$ K^{-1} that is one order of magnitude larger than is found in Ge-doped anti-perovskite manganese nitrates[28] and reduced layered ruthenates.[29] Recent reports on the low temperature phase behavior of δ-FAPbI$_3$ are summarized in Table 1[30–33] including details of the synthesis conditions, sample environment, and cycling temperature that are important in defining the crystal structure. Neutron diffraction experiments and first-principles calculations in FAPbI$_3$ assign the observed phase transitions to

**ADVANCED
SCIENCE NEWS**

www.advancedsciencenews.com

**ADVANCED
MATERIALS**

www.advmat.de
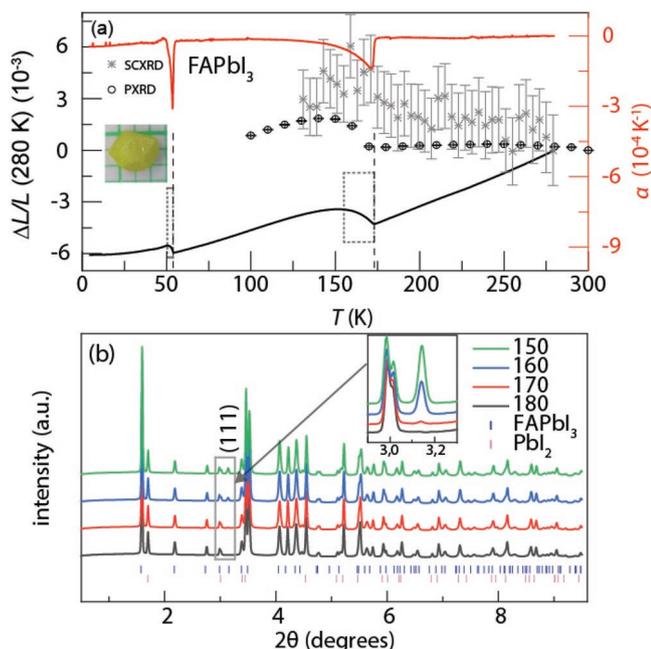
Figure 2. Structural phase transitions and X-ray diffraction pattern in δ-FAPbI$_3$. a) $\Delta L/L$, lattice parameter c (open circles from PXRD, stars from SCXRD), and thermal expansion coefficient α as a function of temperature for δ-FAPbI$_3$. Two regions of NTE are observed below 173 and 54.5 K highlighted by the dashed boxes. b) X-ray diffraction pattern and corresponding Bragg peak locations at 160 K for δ-FAPbI$_3$ (dark blue) and PbI$_2$ (pink) extracted from PXRD measurements.

a change from a hexagonal low temperature (Hex-LT) to a hexagonal intermediate temperature (Hex-IT) phase upon heating the sample whereas via thermal quenching, the cubic phase can be kinetically trapped down to 8 K.[30] Fabini et al.[32] and Sun et al.[33] reported a tetragonal phase, $P4/mbm$, via SCXRD at 285 K and a further transition at 140 K[33] which adopts a low-temperature tetragonal structure. We also note that the high-temperature region of NTE that we observe is correlated with the spectroscopic signature in optical photoluminescence (PL) data where a sudden blueshift of the PL peak attributed to the lattice expansion[34] is observed at temperatures between 120 and 140 K.[10,35] Moreover, it has been shown that ferroelectric domains are formed in the lower symmetry phases at lower temperature,[36,37] which most likely cause the NTE below 54.5 K.

The normalized change of the lattice parameter ($\Delta L/L$(280 K)) in the c-direction, extracted from T-dependent SCXRD measurements, is shown in Figure 2a and confirms the lattice expansion in the same temperature region. However, the total volume of the lattice (displayed in Figure S3 in the Supporting Information) exhibits a steady decrease with decreasing temperature due to a large contraction along the a-axis. Data reduction for $T > 173$ K has been performed using the RT phase, $P6_3/mmc$, while for $T < 173$ K the space group $P6_3/m$ was used. From the PXRD patterns in the proximity of the phase transition, as illustrated in Figure 2b, a new reflection appears at 170 K signaling a phase transition (for full temperature range PXRD waterfall plots see Figure S4, Supporting Information). The phases above and below 170 K were best described by the

space groups $P6_3/mmc$ and $P6_3/m$, respectively, using Le Bail refinement. The result of the refinement at 300 and 160 K can be seen in Figure S5 in the Supporting Information. The new reflection corresponds to the (111) lattice plane in $P6_3/m$ in agreement with the single-crystal precession maps in Figure S6 in the Supporting Information. The evolution of the lattice parameters from PXRD also confirms the presence of the NTE in the c-direction in the same temperature range, accompanied by a large contraction along the a-axis (Figure S7, Supporting Information).

The linear thermal expansion for FAPbBr$_3$ is shown in Figure 3a. In total, three abrupt phase transitions are detected at 120.5, 152, and 161.3 K (Figure 3b–d) with far higher resolution than was achieved in recent measurements of the temperature-dependent dielectric constant.[26] While abrupt changes are seen at 120.5 and 161.3 K, the feature at 152 K has a small shoulder on the low-temperature side as can be seen in $\alpha(T)$. Above 170 K, FAPbBr$_3$ shows two other features with increasing temperature that are illustrated in Figure 3c,d: at around 182 K, $\Delta L(T)/L$ exhibits a small region of NTE with decreasing temperature in a global plateau-like structure. At 265 K, another faint feature is visible. The temperature evolution of the PXRD patterns in FAPbBr$_3$ for two selected ranges of temperature is displayed in Figure 3e,f. The new peaks after the first transition at 250 K were successfully indexed with the space group $P4/mbm$ using a pseudocubic tetragonal cell with the unit cell parameters $a = b \approx \sqrt{2}a_c$ and $c \approx a_c$ where a_c is the lattice constant of the cubic phase. This corresponds to an in-phase octahedral tilt of $a^0a^0c^+$ in Glazer's notation.[38] The full temperature range PXRD waterfall plots are represented in Figure S8 in the Supporting Information. New peaks are marked with asterisks indicating the structural changes around the temperatures observed via dilatometry. The corresponding Bragg peak locations at 250 and 100 K are indicated in Figure 3e,f for FAPbBr$_3$ and PbBr$_2$. To correlate the new peaks that appeared in PXRD, the SCXRD precession maps, as seen in Figure S10 in the Supporting Information, were made. In the precision maps, we identify the appearance of new reflections occurring at 250 K, which indicate phase transitions to a structure with lower symmetry. All reflections including the weak ones were successfully indexed by a pseudocubic tetragonal cell and are in agreement with the systematic absences required by the space group $P4/mbm$. We find that the crystal has undergone twinning during the phase transition with two additional domains rotated 90° with respect to the first domain, aligning the tetragonal c-axes of the two twin domains along the diagonals [110] and [1–10], similar to what is seen in MA-based compounds.[39] Comparing the d-spacings in PXRD and SCXRD represented in Table S3 in the Supporting Information reveals a perfect match. The PXRD and SCXRD results are in agreement with the tetragonal phase suggested by Schueller et al.[25] using PXRD, while Govinda et al.[26] found it to maintain the small cubic structure using SCXRD.

At 100 K, we find an orthorhombic unit cell with $a \approx c \approx \sqrt{2}a_c$ and $b \approx 2a_c$ to give the best description of the superlattice reflection observed in SCXRD. Here the data indicate two twins rotated 120° around the [0–11] and [110] directions. The precession maps in Figure S11 in the Supporting Information
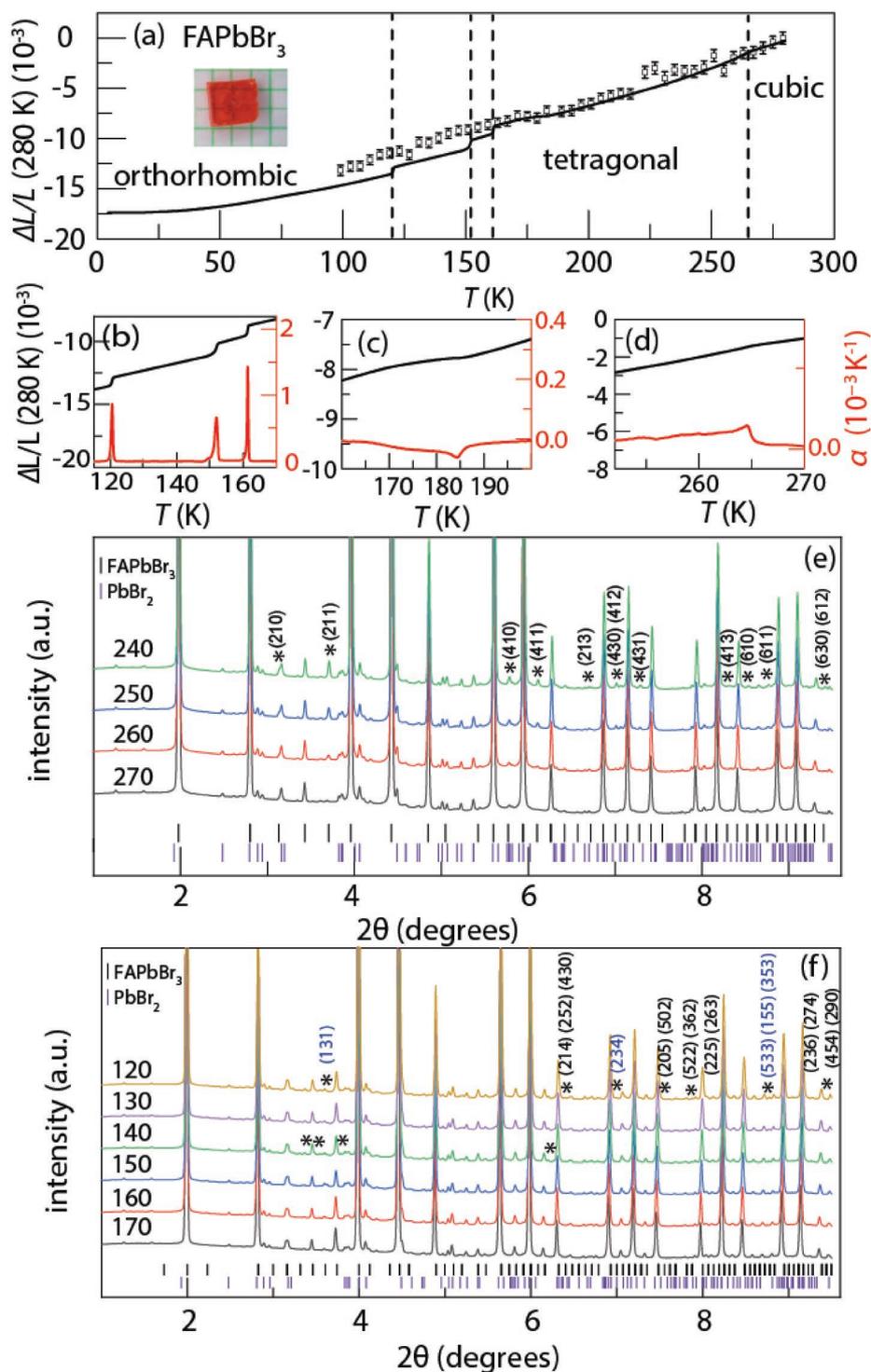
Figure 3. Structural phase transitions and X-ray diffraction pattern in FAPbBr$_3$. a) $\Delta L/L$ and lattice parameter a (open circles) as a function of temperature: in $\Delta L/L$, a cascade of sharp phase transition between 120 and 165 K and a continuously increasing background is observed with increasing temperature. The dashed lines indicate strong changes in $\Delta L/L$. b–d) $\Delta L/L$ and α in different ranges of temperature. e,f) PXRD pattern in the high (e) and low (f) temperature range (text in blue = observed in both PXRD/SCXRD, text in black = not observed in SCXRD). New peaks are marked with asterisks. The corresponding Bragg peak locations at 250 and 100 K are indicated in (e) and (f) for FAPbBr$_3$ and PbBr$_2$.

calculated with this cell are in agreement with the space group *Pnma*. However, this space group does not describe all of the new reflections appearing in the PXRD between 130 K and

170 K as shown in Figure 3f. This points toward a lower symmetry than reported by Schueller et al.[25] Several of the indexed reflections in PXRD did not show intensity in the SCXRD

Table 1. Summary of the structural phase transitions with increasing temperature observed in $FAPbI_3$.

FAPbI₃	Transition/abrupt changes in $\Delta L/L$	Phase	Lattice parameters		Space group	Synthesis method
			a [Å]	c [Å]		
Ref. [30] (Neutron powder diffraction)	15 K	Hexagonal-LT	8.5070	7.9505	$P6_3/m$	Solution process/ precipitation
	220 K	Hexagonal-IT	8.6226	7.9458	$P6_3/mmc$	
	390 K	Cubic	6.3855	6.3855	$Pm3m$	
Ref. [31] (SCXRD)	150 K	Trigonal	17.7914	10.9016	$P3m1$	Inverse temperature crystallization
	293 K	Trigonal	8.9817	11.006	$P3$	
Ref. [32] (PXRD)	285 K	Tetragonal	8.92276	6.32626	$P4/mbm$	Solution process/ precipitation
Ref. [33] (SCXRD)	140 K	Tetragonal	8.87516	6.27916	$P4/mbm$	Inverse temperature crystallization
	285 K	Tetragonal	8.92276	6.32626	$P4/mbm$	
Present work (thermal expansion and SCXRD/PXRD)	54.5 K	–	–	–	–	Inverse temperature crystallization
	173.0 K	Hexagonal	8.5900 (PXRD value)	7.93289 (PXRD value)	$P6_3/m$	

data. A few of the reflections have not been found in SCXRD, presumably due to the extremely low intensity of some of the superlattice reflections. The comparison between the *d*-spacings of the lattice plane found in both PXRD and SCXRD show a good match, see Table S4 in the Supporting Information.

To conclude, we have presented an investigation of the linear thermal expansion of bulk single crystals of lead-halide perovskites in the temperature range between 4.2 and 280 K supported by transport measurements and experiments under steady-state illumination for MA-based perovskites. Solid evidence for structural phase transitions superimposed on a smoothly varying background was uncovered for all compounds, though its overall shape depends strongly on the individual material. We observe that FA-based HOIPs exhibit a variety of interesting properties such as two regions of NTE (δ-FAPbI$_3$) with a large NTE coefficient and a cascade of sharp transitions (FAPbBr$_3$) with decreasing temperature. With temperature-dependent PXRD, we have identified the corresponding phases for the FA-based compounds. For FAPbBr$_3$, the symmetry changes identified by XRD data analysis are linked to the tilting of the PbBr$_6$ octahedra. These unexpected observations underline the strength of thermal expansion experiments to probe the lattice parameters and to precisely determine the structural phase transition temperatures. Since any structural change has severe impact on the phononic and electronic structure, the information provided by this study can be employed strategically to predict changes in the optical and charge transport properties that are currently under intense investigation. It is noteworthy that the structural phase transitions for HOIPs of different cations are analogous; meaning most findings of phase transitions can be translated, with generally just a shift in the temperature scale as a function of Goldschmidt's tolerance factors. This information extends across temperatures above room temperature for some other HOIP relatives.

Experimental Section

Device Synthesis and Characterization: All bulk single crystals with flat facets up to 4 × 4 mm² and a thickness of around $L = 1$ mm were grown using the inverse temperature crystallization method, as reported in the literature.[40,41] For all the results mentioned above the freshly synthesized crystals were used unless indicated. For transport experiments, Au was evaporated on the sample edges either in a four- or six-terminal configuration (in van der Pauw or in Hall/bar geometry) and Au wires with a diameter of 25 µm were attached by means of Ag conductive paste to the sample that had been mounted on a chip carrier.[16]

Table 2. Summary of the structural phase transitions with increasing temperature observed in $FAPbBr_3$.

FAPbBr₃	Transition/ abruptchanges in $\Delta L/L$	Phase	Lattice parameters			Space group	Synthesis method
			a [Å]	b [Å]	c [Å]		
Ref. [25] (PXRD)	100 K	Orthorhombic	8.37433	11.8609	8.38073	$Pnma$	Solution process/precipitation
	175 K	Tetragonal	8.41525		5.94735	$P4/mbm$	
	275 K	Cubic	5.98618			Pm-$3m$	
Ref. [26] (SCXRD)	100 K	Trigonal	8.3470	8.3470	10.2180	R-3	Inverse temperature crystallization
	185 K	Cubic	5.9582	5.9582	5.9582	Pm-$3m$	
	295 K	Cubic	6.0134	6.0134	6.0134	Pm-$3m$	
Present work (thermal expansion and SCXRD)	120.5 K	Orthorhombic	8.38742	11.8546	8.37959	$Pnma$	Inverse temperature crystallization
	152.0 K	Tetragonal	8.441622		5.94989	$P4/mbm$	
	170 K	Cubic	5.98730			Pm-$3m$	
	265.0 K						

Thermal Expansion Experiments: Thermal expansion measurements were carried out using a high-resolution (down to 0.02 Å) capacitive dilatometer.[19,20] The dilatometer cell was made from a CuBe alloy and was attached to a specifically designed probe.[20] This probe was put into a vacuum tube and filled with a sufficient amount of ^{4}He contact gas to ensure thermal equilibrium during the measurement. All thermal expansion curves were recorded during the warm up (with a maximum warm up time of 72 h) to ensure quasi-adiabatic conditions. The length change ΔL of the sample along the main axis was measured using an ultrahigh-resolution Andeen–Hagerling capacitance bridge (AH2500). The absolute values of capacitance were always kept between 15 and 25 pF.

Magneto-Transport Experiments: A special probe that is equipped with an optical fiber, a calibrated Cernox thermometer, and a strain gauge heater was employed to monitor the temperature. The probe was placed in a vacuum tube, equipped with an additional inner vacuum chamber to perform transport experiments from 4.2 to 300 K, in the presence of a small amount of ^{4}He contact gas. The temperature was monitored using a standard Lakeshore temperature controller. The AC measurements were performed using a Keithley 6221 current source at frequencies around 13 Hz and Stanford 830 Lock-in amplifiers with suitable preamplifiers. The applied excitation current varied between 10 nA and 1 μA (always in the Ohmic regime). A solid-state laser (373 nm) was utilized for the photoconductivity measurements at a fixed power of 5 mW.[16]

Temperature-Dependent SCXRD Measurements: Temperature-dependent single-crystal diffraction data were collected on an Oxford Diffraction Supernova diffractometer using a Mo Kα source (λ = 0.71073 Å) operated at 50 kV and 0.80 mA and a detector distance of 73 mm. FAPbX$_3$ single crystals with dimensions ≈ 40 × 40 × 10 (μm)^3 were selected and mounted on a goniometer head using paratone-N oil. The crystals were cooled between 280 and 100 K using an Oxford Cryosystems Cryostream 700 device. Data were collected in steps of 2 K and the temperature was allowed to equilibrate for 1–2 min prior to data collection. The collection strategy used allowed for 100% completeness of the *Pm*-3*m* space group for FAPbBr$_3$ and *P*6$_3$/*m* for FAPbI$_3$ with an exposure time of 7 s per frame. The program CrysalisPro32 was used to control the data collection and for the subsequent data reduction. The fitted lattice parameters were averaged in pairs of two in order to reduce errors introduced by small variations in the goniometer head placement at the start of each temperature increment.

Data for precession maps were collected on a Bruker APEX2 diffractometer with an Ag X-ray source (λ = 0.56086 Å) operated at 50 kV and 0.88 mA with a detector distance of 45 mm. The same crystals were used for the temperature scan. Five ω settings were selected combined with ϕ scans with a 90 s exposure time per degree for a total of 16 h. The crystals were cooled at 360 K h^{-1} between each measurement at 280, 250, and 100 K using an Oxford Cryosystems Cryostream 700 device. Collection and reduction were carried out in the APEX3 software.

Temperature-Dependent PXRD Measurements: Capillaries were mounted on the sample spinner at beamline P02.1 (PETRA III, DESY, Hamburg, Germany).[42] An initial diffraction pattern of the sample was collected at room temperature using a PerkinElmer XRD1621 area detector at a wavelength of 0.20684 Å. The sample was cooled directly to 100 K, using an Oxford Cryosystems Cryostream 700 device, and then warmed in 10 K steps to 300 K, with diffraction patterns collected at each step. Finally, the sample was cooled to 110 K with diffraction patterns again collected at 10 K intervals. Diffraction data were calibrated and integrated using the routines available within the DAWN suite.[43] LeBail fits were performed using FullProf.[44]

Fluorescence Lifetime Imaging: A 488 nm pulsed diode laser was employed as excitation source which was set at a repetition rate of 10 MHz. The corresponding excitation laser beam was directed into the crystals through an oil immersion objective (100 × 1.4 NA) of an inverted microscope system. The fluorescence light was collected back and filtered by the main dichroic and cut-off filters. The fluorescence photons were detected by an avalanche photodiode (SPCM-AQR-14, Perkin–Elmer). Photon counting and time tagging were performed within a TimeHarp 200 module (PicoQuant), with a time resolution of 29 ps per channel. The FLIM images were analyzed using SymphoTime 32 software (PicoQuant).

Supporting Information

Supporting Information is available from the Wiley Online Library or from the author.

Conflict of Interest

The authors declare no conflict of interest.

[1] M. A. Green, A. Ho-Baillie, H. J. Snaith, *Nat. Photonics* **2014**, *8*, 506.

[2] N. J. Jeon, J. H. Noh, W. Seok Yang, Y. C. Kim, S. Ryu, J. Seo, S. Il Seok, *Nature* **2015**, *476*, 517.

[3] M. A. Green, K. Emery, Y. Hishikawa, W. Warta, E. D. Dunlop, *Prog. Photovoltaics* **2015**, *1*, 23.

[4] National Renewable Energy Laboratory (NREL) https://www.nrel.gov/pv/assets/images/efficiency-chart-20180716.jpg (accessed: July 2018).

[5] V. D'Innocenzo, G. Grancini, M. J. P. Alcocer, A. R. S. Kandada, S. D. Stranks, M. M. Lee, G. Lanzani, H. J. Snaith, A. Petrozza, *Nat. Commun.* **2014**, *5*, 3586.

[6] L. M. Herz, *Annu. Rev. Phys. Chem.* **2016**, *67*, 65.

[7] M. M. Lee, J. Teuscher, T. Miyasaka, T. N. Murakami, H. J. Snaith, *Science* **2012**, *338*, 643.

[8] S. D. Stranks, G. E. Eperon, G. Grancini, C. Menelaou, M. J. P. Alcocer, T. Leijtens, L. M. Herz, A. Petrozza, H. J. Snaith, *Science* **2013**, *342*, 341.

[9] Y. Chen, H. T. Yi, X. Wu, R. Haroldson, Y. N. Gartstein, Y. I. Rodionov, K. S. Tikhonov, A. Zakhidov, X.-Y. Zhu, V. Podzorov, *Nat. Commun.* **2016**, *7*, 12253.

ADVANCED
SCIENCE NEWS
www.advancedsciencenews.com

ADVANCED
MATERIALS
www.advmat.de

[10] H.-H. Fang, R. Raissa, M. Abdu-Aguye, S. Adjokatse, G. R. Blake, J. Even, M. A. Loi, *Adv. Funct. Mater.* **2015**, *25*, 2378.

[11] T. Zhao, W. Shi, J. Xi, D. Wang, Z. Shuai, *Sci. Rep.* **2016**, *7*, 19968.

[12] A. Miyata, A. Mitioglu, P. Plochocka, O. Portugall, J. Tse-Wei Wang, S. D. Stranks, H. J. Snaith, R. J. Nicholas, *Nat. Phys.* **2015**, *11*, 582.

[13] K. Galkowski, A. Mitioglu, A. Miyata, P. Plochocka, O. Portugall, G. E. Eperon, J. Tse-Wei Wang, T. Stergiopoulos, S. D. Stranks, H. J. Snaith, R. J. Nicholas, *Energy Environ. Sci.* **2016**, *9*, 962.

[14] Z. Yang, A. Surrente, K. Galkowski, N. Bruyant, D. K. Maude, A. Abbas Haghighirad, H. J. Snaith, P. Plochocka, R. J. Nicholas, *J. Phys. Chem. Lett.* **2017**, *8*, 1851.

[15] H. T. Yi, X. Wu, X. Zhu, V. Podzorov, *Adv. Mater.* **2016**, *28*, 6509.

[16] M. Keshavarz, S. Wiedmann, H. Yuan, E. Debroye, M. Roeffaers, J. Hofkens, *ACS Energy Lett.* **2018**, *3*, 39.

[17] A. Poglitsch, D. J. Weber, *Chem. Phys.* **1987**, *87*, 6373.

[18] N. Onoda-Yamamuro, T. Matsuo, H. Suga, *J. Phys. Chem. Solids* **1990**, *51*, 1383.

[19] R. Küchler, T. Bauer, M. Brando, F. Steglich, *Rev. Sci. Instrum.* **2012**, *83*, 095102.

[20] R. Küchler, A. Wörl, P. Gegenwart, M. Berben, B. Bryant, S. Wiedmann, *Rev. Sci. Instrum.* **2017**, *88*, 083903.

[21] M. T. Weller, O. J. Weber, P. F. Henry, A. M. Di Pumpoa, T. C. Hansen, *Chem. Commun.* **2015**, *51*, 4180.

[22] F. Brivio, J. M. Frost, J. M. Skelton, A. J. Jackson, O. J. Weber, M. T. Weller, A. R. Goni, A. M. A. Leguy, P. R. F. Barnes, A. Walsh, *Phys. Rev. B* **2015**, *92*, 144308.

[23] P. S. Whitfield, N. Herron, W. E. Guise, K. Page, Y. Q. Cheng, I. Milas, M. K. Crawford, *Sci. Rep.* **2016**, *6*, 35685.

[24] C. Ge, M. Hu, P. Wu, Q. Tan, Z. Chen, Y. Wang, J. Shi, J. Feng, *J. Phys. Chem. C* **2018**, *122*, 15973.

[25] E. C. Schueller, G. Laurita, D. H. Fabini, C. C. Stoumpos, M. G. Kanatzidis, R. Seshadri, *Inorg. Chem.* **2018**, *57*, 695.

[26] S. Govinda, B. P. Kore, D. Swain, A. Hossain, C. De, T. N. Guru Row, D. D. Sarma, *J. Phys. Chem. C* **2018**, *122*, 13758.

[27] K. Takenaka, *Sci. Technol. Adv. Mater.* **2012**, *13*, 013001.

[28] K. Takenaka, H. Takagi, *Appl. Phys. Lett.* **2005**, *87*, 261902.

[29] K. Takenaka, Y. Okamoto, T. Shinoda, N. Katayama, Y. Sakai, *Nat. Commun.* **2017**, *8*, 14102.

[30] T. Chen, B. J. Foley, C. Park, C. M. Brown, L. W. Harriger, J. Lee, J. Ruff, M. Yoon, J. J. Choi, S.-H. Lee, *Sci. Adv.* **2016**, *160*, 1650.

[31] C. C. Stoumpos, C. D. Malliakas, M. G. Kanatzidis, *Inorg. Chem.* **2013**, *52*, 9019.

[32] D. H. Fabini, C. C. Stoumpos, G. Laurita, A. Kaltzoglou, A. G. Kontos, P. Falaras, M. G. Kanatzidis, R. Seshadri, *Angew. Chem., Int. Ed.* **2016**, *55*, 15392.

[33] S. Sun, Z. Deng, Y. Wu, F. Wei, F. H. Isikgor, F. Brivio, M. W. Gaultois, J. Ouyang, P. D. Bristowe, A. K. Cheetham, G. Kieslich, T. B. Bein, H. J. Snaith, R. H. Friend, H.-K. Mao, *Chem. Commun.* **2017**, *53*, 7537.

[34] D. H. Fabini, G. Laurita, J. S. Bechtel, C. C. Stoumpos, H. A. Evans, A. G. Kontos, Y. S. Raptis, P. Falaras, A. Van der Ven, M. G. Kanatzidis, R. Seshadri, *J. Am. Chem. Soc.* **2016**, *138*, 11820.

[35] Y. Kutes, L. Ye, Y. Zhou, S. Pang, B. D. Huey, N. P. Padture, *J. Phys. Chem. Lett.* **2014**, *5*, 3335.

[36] A. D. Wright, C. Verdi, R. L. Milot, G. E. Eperon, M. A. Pérez-Osorio, H. J. Snaith, F. Giustino, M. B. Johnston, L. M. Herz, *Nat. Commun.* **2016**, *7*, 11755.

[37] Y. Rakita, O. Bar-Elli, E. Meirzadeh, Y. Peleg, G. Hodes, I. Lubomirsky, D. Oron, D. Ehre, D. Cahen, *Proc. Natl. Acad. Sci. USA* **2017**, *114*, E5504.

[38] A. M. Glazer, *Acta Crystallogr., Sect. B: Struct. Crystallogr. Cryst. Chem.* **1972**, *28*, 3384.

[39] M. Szafrański, A. Katrusiak, *J. Phys. Chem. Lett.* **2017**, *8*, 2496.

[40] M. I. Saidaminov, A. L. Abdelhady, B. Murali, E. Alarousu, V. M. Burlakov, W. Peng, I. Dursun, L. Wang, Y. He, G. Maculan, A. Goriely, T. Wu, O. F. Mohammed, O. M. Bakr, *Nat. Commun.* **2015**, *6*, 7586.

[41] A. A. Zhumekenov, M. I. Saidaminov, M. Azimul Haque, E. Alarousu, S. P. Sarmah, B. Murali, I. Dursun, X.-H. Miao, A. L. Abdelhady, T. Wu, O. F. Mohammed, O. M. Bakr, *ACS Energy Lett.* **2016**, *1*, 32.

[42] A.-C. Dippel, H.-P. Liermann, J. T. Delitz, P. Walter, H. Schulte-Schrepping, O. H. Seeck, H. Franz, *J. Synchrotron Radiat.* **2015**, *22*, 675.

[43] J. Filik, A. W. Ashton, P. C. Y. Chang, P. A. Chater, S. J. Day, M. Drakopoulos, M. W. Gerring, M. L. Hart, O. V. Magdysyuk, S. Michalik, A. Smith, C. C. Tang, N. J. Terrill, M. T. Wharmby, H. Wilhelm, *J. Appl. Crystallogr.* **2017**, *50*, 959.

[44] J. Rodrigues-Carvajal, *Comm. Powder Diffr. IUCr Newsl.* **2001**, *26*, 12.